photonics

MDPI

Article

Femtosecond Laser-Induced Ultrafast Electron Redistribution near a Microscale Metallic Filament

Dacai Liu [1,2,3] and Bin Li [1,2,3,4,*]

[1] Shanghai Institute of Applied Physics, Chinese Academy of Sciences, Shanghai 201800, China; liudacai@sinap.ac.cn
[2] Shanghai Synchrotron Radiation Facility, Shanghai Advanced Research Institute, Chinese Academy of Sciences, Shanghai 201204, China
[3] University of Chinese Academy of Sciences, Beijing 100049, China
[4] School of Physical Science and Technology, Shanghai Tech University, Shanghai 201210, China
* Correspondence: libin1995@sinap.ac.cn

Abstract

In this study, a femtosecond laser beam is delivered to metal wire targets to generate suprathermal electron jets reaching energies of several hundreds of keV. During the process, it is observed that the mirror-imaging distribution of the beam focus with respect to the surface of the target displays highly asymmetric features and different dynamic responses. Especially, the exterior focus exhibits an extraordinary polarity reversal of the macroscopic current, while the interior focus behaves ordinarily. The former is attributed to the strong field at the focal point outside the surface, causing the secondary ionization and driving electrons back to the target, thereby reshaping the distribution of these high-energy hot electrons and the morphology of plasma jets. A numerical model is proposed to simulate the experimental observation and interpret the unexpected phenomenon. Furthermore, the particle-in-cell algorithm is also implemented to verify the results and present more details. This study seeks to emphasize the role of focal position in regulating the photoemission process, which may offer a fresh perspective for research in laser–material interactions and dynamics.

Keywords: laser–metal interaction; metallic filament; laser beam focus; plasma dynamics; particle-in-cell (PIC) simulation; tunnelling ionization

1. Introduction

Since the invention of the chirped pulse amplification (CPA) technique [1], the interaction between intense laser pulses and metals has been extensively investigated [2–7]. In these studies, the behaviour of photoemitted suprathermal electrons with energies reaching hundreds of keV, and the evolutionary dynamics of plasmas have become the central topics. Those high-energy suprathermal electrons not only serve as the key energy carriers in inertial confinement fusion schemes, e.g., "fast ignition", but also drive the secondary radiation sources (e.g., ultrafast X-rays) and high-energy particle beams, demonstrating broad application prospects. Notable phenomena and experiments include laser-induced metallic plasma jets [8–10], novel electron sources based on laser-irradiated metal wires [11–14], wire-target plasma devices for fusion ignition [15–17], laser-driven collimated electron emission along wire [11,12,18–20], the generation of strong sub-terahertz surface waves on metal wires [21–24], and intense terahertz radiation from femtosecond-laser-driven wire-

Check for updates

Received: 11 March 2026
Revised: 10 April 2026
Accepted: 14 April 2026
Published: 24 April 2026

Copyright: © 2026 by the authors. Licensee MDPI, Basel, Switzerland. This article is an open access article distributed under the terms and conditions of the Creative Commons Attribution (CC BY) license.

guided helical undulators [25]. Among these, the wire-based electron or radiation sources have demonstrated considerable potential applications, attracting accumulating interest.

In the meantime, theoretical investigations of laser–solid–plasma interactions have also been conducted. For example, Kluge et al. studied absorption mechanisms and hot electron generation in laser-produced plasmas [26]. Keldysh developed the ionization theory under the strong laser field approximation [27]. Later, more complete mathematical algorithms were proposed based on Keldysh theory [27]. A. Kasperczuk et al. employed X-ray interferometric imaging to study the influence of focal position on plasma jet morphology and electron density distribution in a defocused laser system [28]. Zhang et al. observed the photoemission current change at various positions outside the laser ablation spot. For the past decades [29], with the development and establishment of laser–solid interaction and radiation absorption mechanism [30–32], the understanding of laser–metal ionization becomes deeper and clearer [33–38]. However, these studies are primarily focused on the influence due to the laser beam intensity without regarding the beam focal position as a critical parameter. The subtle feature related to the current flow and beam distribution around the target is lacking in investigation, and the relevant simulation model is yet to be established [39,40]. In order to unveil the underlying microscopic mechanism of ultrafast electron redistribution, which has not been addressed in previous works, it triggers our motivation to elucidate the backflow dynamics and evolution process of suprathermal electrons in the vicinity of a microscopic metal wire, and to reveal the physics insight.

2. Materials and Methods

The experimental set-up is illustrated in Figure 1A Yb: CaF_2 laser amplifier delivering a pulse energy of 5 mJ at 100 Hz repetition frequency, with a central wavelength of 1030 nm and a pulse duration of 400 fs (FWHM) is employed. The laser beam was expanded and then focused down to a spot size of 10 μm, achieving a peak intensity exceeding 5×10^{17} W/cm^2. A half-wave plate combining a polarization cube is used to tune the pulse energy for the experiment while monitoring the shot-by-shot energy fluctuation simultaneously. A CCD camera is employed to take shots, imaging and calibrating the laser beam spot during the translation stage scan. Due to the tilted orientation of the metal wire (with respect to the axis of the motion), the beam waist (focal spot) could be accurately identified as it is positioned on the target surface. According to the coordinates of the translation stage, the relative position between the focal spot and the target surface could be readily derived and determined via optical geometry. The suprathermal electron energy is diagnosed using an online electron time-of-flight (e-TOF) energy spectrometer. The wire photoemission experiment is conducted within a vacuum chamber under a base pressure better than 1×10^{-4} Pa and at a constant ambient temperature of 25 °C.

Copper or tungsten wires with a diameter of 300 μm were used as target materials. In each experimental run, a wire target was mounted on a high-precision in-vacuum manipulation stage via an insulating ceramic holder, providing translational accuracy of ~0.1 μm and rotational accuracy of 10 μrad respectively. The laser beam propagates towards the metal wire approximately perpendicular within the interaction region, while the translation direction of the scanning stage was oriented at an angle of 10° relative to the wire axis. Thus, when the wire scans along with the stage, the relative position of the laser beam focus with respect to the wire surface would change during the motion, i.e., the scan of the translation stage in the x-direction Δx leads to the tuning of the focal spot in the z-direction $\Delta z = \Delta x \cdot tan10°$. Here '−' is used to denote the focus moving towards inside the material, and '+' to denote moving outside. As the focus of the laser beam is scanned from inside to outside the wire, highlighted by the various positions along the z-axis, −90 μm, 0 μm, 193 μm, 385 μm, the generated back-loop current, i.e., the photoemitted

electron current, is measured simultaneously using a shielded cable connected via a vacuum feedthrough to a picoammeter. The experimental error could be carried out, which is primarily attributed to the laser energy fluctuation and the measurement uncertainty of the picoammeter. To characterize the stability of our system, the backflow current fluctuation was measured at a unique beam size, demonstrating that the peak-to-valley (PV) fluctuation remained ±5% within the average value.

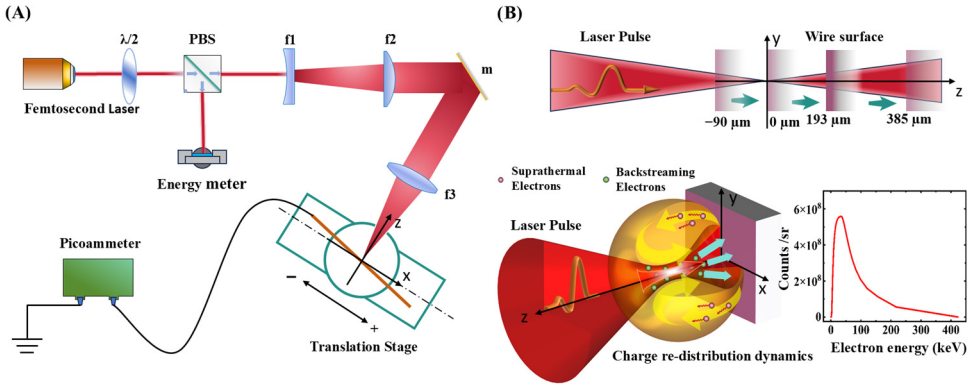

Figure 1. The schematic diagram shows the experimental setup for laser focusing near a metallic filament to induce photo-electron emission and back-loop current. (**A**) A femtosecond laser beam is expanded by a f1:f2 telescope system and then focused by f3 lens to achieve a focal spot of 10 μm near a 300 μm diameter metal wire, which is fixed on a translation stage, having an intersection angle of 10° with the direction of motion. A picoammeter is utilized to measure the back-loop current during the experiment. (**B**) The laser beam is stationary, as the wire scans along its axis approximately, the beam focus would move across the wire, which leads to the separation between the focal spot and the wire surface ranging from −90 μm to 385 μm. Especially when the focal spot is located exterior to the wire, the emitted super-thermal electrons with several tens to hundreds of keV would turn around and be driven back to the surface. This unexpected phenomenon is due to the local laser field near the beam waist, causing the charge redistribution around the wire. The inserted red curve represents a typical hot electron energy spectrum measured by an electron time-of-flight (e-TOF) energy spectrometer.

3. Results and Discussion

Figure 2 displays the femtosecond laser-induced photoemission current for both copper (Cu) and tungsten (W) wires. When scanning the translation stage, it would change the beam focal position relative to the wire surface (in Figure 1B). The net photoemission current for both Cu and W wires measured at the orientation angle of 10° is shown and compared (Figure 2C). Meanwhile, the control signal acquired at 0° angle for W is sketched in the same plot (Figure 2B), where the focus remains precisely on the surface during the scan, and the measured current is close to a constant. In contrast, the signals for both Cu and W wires at 10° undergo significant change. As the focus moves from the interior towards the surface of the wire (z-position changes from −90 μm to 0 μm), the excitation current increases, reaching the positive maximum when the focus is on the surface, corresponding to the laser beam's peak intensity. For the Cu case, as the beam waist moves away from the surface to the exterior region (z-position 0 μm to 193 μm), the current starts to decrease monotonously and changes sign at a certain distance, attaining a pronounced negative value. It indicates that, within this stage, the metal wire temporarily acquires electrons and reverses the direction of the net-charge flow. However, this trend wouldn't continue all the time. At the z-position 193 μm and beyond, the current stops to become more negative, instead gradually returns to net-zero up to z-position 385 μm, and then turns to a small but positive value when the focus moves further away, restoring the regular photoemission. The above phenomenon, particularly the reversal feature of the net change flow in the

microscale wire under the laser pulse illumination, challenges the conventional expectation and suggests a potential new dynamic algorithm for the electron redistribution.

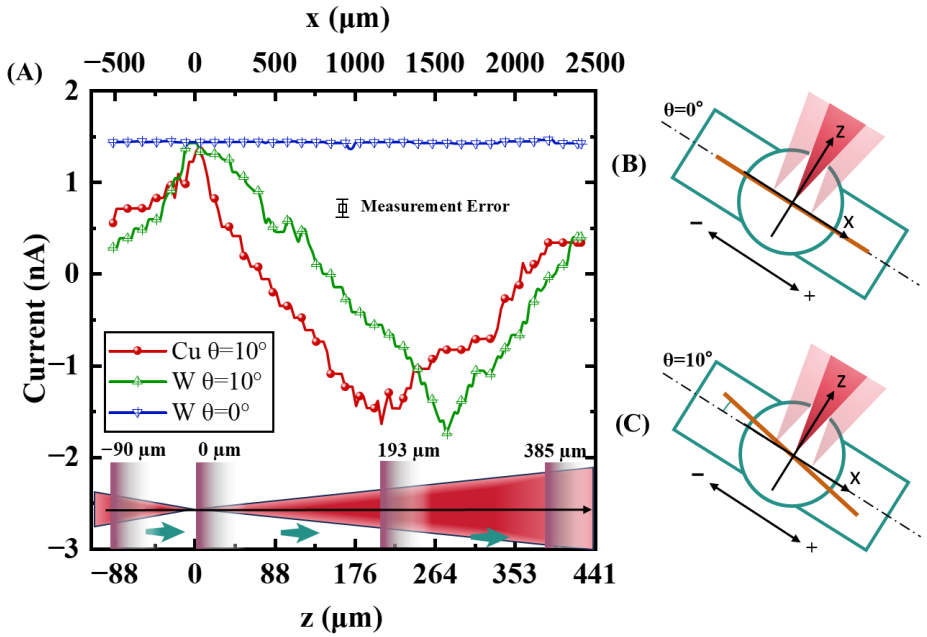

Figure 2. The experimental results of the back-loop current due to the femtosecond laser illumination of the metallic filament. (**A**) The red and green curves represent the measured current for copper (Cu) and tungsten (W), respectively, employing the geometry in (**C**), while the blue curve represents the control signal for W employing the geometry in (**B**), where the beam focus remains on the surface of the wire during the scanning motion. The average measurement error is denoted by an inserted icon. More details regarding the wire scanning geometry (**B**,**C**) are presented in the main text.

To elucidate the underlying physics, data analysis is further conducted, and a numerical simulation model is developed. The scanning motion of the translation stage causes the change in the focal position along the z-direction, thus the laser beam intensity at the surface varies as:

$$I_s = \frac{I_p}{1 + (z/z_R)^2} \tag{1}$$

where I_p denotes the peak intensity at the beam waist, z_R is the Rayleigh length, and z represents the distance from the focus to the surface. The curvature of the wire surface is neglected, i.e., being treated as a flat plane, since the beam focal size (~10 μm) is much smaller than the wire diameter (300 μm). Considering the beam intensity in the experimental regime, the dominant ionization processes can be categorized into three types of dynamics: multiphoton ionization (MPI), tunnel ionization (TI), and over-the-barrier ionization (OBI). Thus, the Keldysh parameter γ [27] could be rewritten as:

$$\gamma = \omega \sqrt{\frac{E_0 c \epsilon_0 (1 + z^2/{z_R}^2)}{I_p}} \tag{2}$$

where ω is the angular frequency of the laser, E_0 is the ionization energy of the material in wire, c is the speed of light, and ϵ_0 is the vacuum permittivity. So $\gamma \gg 1$ corresponds to the typical multiphoton absorption regime, while $\gamma \ll 1$, tunnel ionization would dominate [30–32]. In Figure 3A, the specific contribution from the aforementioned three dynamics versus the beam intensity on the surface in the experiment is depicted.

And the ionization rate from the surface w_{out} could be calculated and expressed in terms of γ [27]:

$$w_{out} = \frac{\sqrt{6\pi}}{2} \times \sqrt{\frac{E_0\omega}{\gamma}} \exp\left(-\frac{4}{3}\frac{E_0\gamma}{\omega}[1-\frac{1}{10}\gamma^2]\right) \quad (3)$$

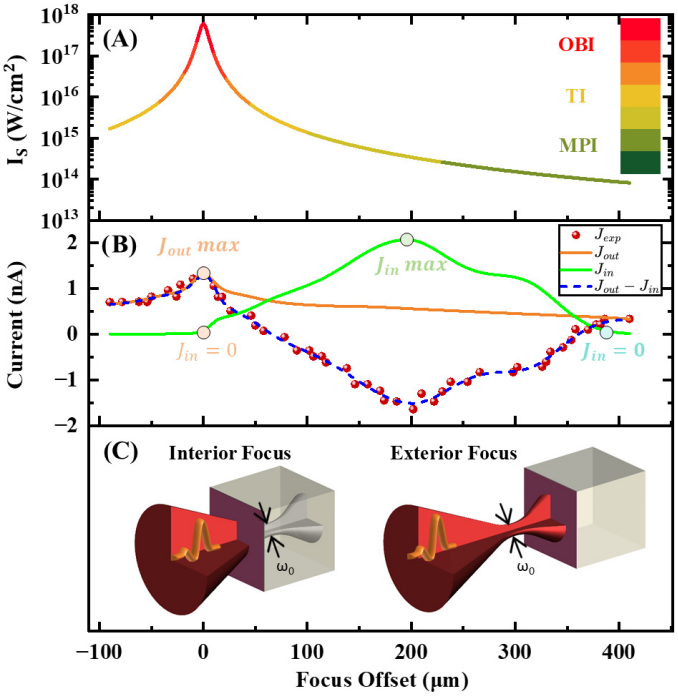

Figure 3. Theoretical simulation to illustrate various dynamic processes during the laser pulse irradiation of the metal wire, and the simulated results are compared with the experiment. The process could be described by our simulation model, including three dynamic processes: "−90 μm to 0 μm" shows that, as the laser focus moves from the interior to the copper surface, the photoemission current (J_{out}: outward flow) increases, reaching the peak value at the surface; "0−193 μm" displays, the focus moves away from the surface to a certain distance outside, where the return current (J_{in} : inward flow) starts to increase to its maximum; and finally, "193–385 μm" corresponds to the case for the focus moving further away, the inward flow current attenuates, then the net outward flow recovers. (**A**) The red, yellow, and green divisions of the curve represent the over-the-barrier ionization (OBI), tunnel ionization (TI), and multiphoton ionization (MPI) regimes respectively, and the corresponding laser beam intensities on the surface I_s are shown. (**B**) The measurement results for the net current during the scan motion are given by a solid circle in red. A simulation algorithm is developed to interpret the result. The orange curve corresponds to the normal outward excitation current (J_{out}), and the green curve is associated with the unexpected backflow current (J_{in}) due to the electrons pulled back by the drag force of the exterior beam focus, and the blue dashed line gives the difference between them ($J_{out} - J_{in}$), which is well comparable with the net current result measured in the experiment. (**C**) The schematic exhibits the mirror-imaging geometry for the laser beam focus located interior or exterior with respect to the surface of the metal filament.

Moreover, in the experimental beam intensity range, the theory of ultra-intense laser–solid interactions [33–38] is implemented to calculate the laser absorption by the target, mainly involving four mechanisms: vacuum heating (VH), resonance absorption (RA), inverse bremsstrahlung (IB) absorption, and J × B absorption. The competition among these mechanisms varies with beam intensity, making it difficult to determine the absolute absorption efficiency directly. Then, as illustrated in Figure 3B, the total net current in copper wire excited by the laser pulse could be deconvoluted into two components: J_{out} and J_{in}, where J_{out} represents the regular current directly excited by the laser at the metal surface, emitting outward from the surface, while J_{in} denotes the current flowing inward

to the surface. The latter is regarded as the primary cause of the unexpected macroscopic current reversal observed in our experiment, and it is mainly due to the electron population being pulled back to the surface by the drag force from the beam focus located exterior to the wire (refer to Figure 1B). During the process for the laser focus moving from the interior to the surface, $J_{in} = 0$, and J_{out} should be symmetric around the focus in the z-direction. At this stage, the outward excitation efficiency f_{out} can be inversely fitted using the back-loop current data for z = −90 μm to 0 μm. Incorporating the factor f_{out} and the ionization rate w_{out}, J_{out} is calculated:

$$J_{out} = ew_{out}f_{out}\tau f_{rep} \quad (4)$$

where e is the electron charge, τ and f_{rep} represent the pulse duration and repetition frequency of the laser respectively. Via this scheme, J_{out} values at various positions can be calculated, and shown as the red curve in Figure 3B.

In the following section, let us turn to the analysis of J_{in}, and explore its origin. During the process for z = 0 μm to 193 μm, the focus moves away from the surface into the space. Within this stage, the beam focus remains relatively close to the surface, and a significant population of electrons and ions is generated and persists near the interaction point (the beam focus). Especially, the ions evaporated from the surface would undergo the secondary ionization under the intense field strength of the laser pulse, liberating a large number of new electrons, which are then pulled back towards the surface along the laser propagation direction. This makes the net current of the wire reverse to a negative value, and explains where J_{in} comes from.

Using Equations (2) and (3) and considering the laser beam intensity at various z positions, the secondary ionization rate at the exterior beam focus w_{in} can be calculated and the algorithm is depicted in Figure 1B. Referring to the laser–plasma absorption theory [40], the dominant mechanism is expected to be J × B absorption primarily, with absorption efficiency $f_{in} \approx f_{jb} \propto \sqrt{1 + \frac{I_p\lambda^2}{1.37\times10^{18}}} - 1$. So the magnitude of the backflow (inward flow) current can be calculated by:

$$J_{in} = ew_{in}\tau f_{rep}f_{in}R_k \quad (5)$$

where R_k denotes the factor $1/\left(1 + (z/z_R)^2\right)$, w_{in} is defined previously as the ionization excitation rate at the focal point (refer to supplemental materials for more details). Apparently, the ionization rate w_{in} would influence the magnitude of J_{in}, which changes the overall surface ionization mechanism, showing asymmetric features for the interior and exterior focal conditions, referring to Figure 3C.

During the process for z position 193–385 μm, as the focus moves further away, R_k decreases rapidly, leading to J_{in} diminishing gradually down to nearly zero; J_{out} would decrease concurrently since the laser intensity diminishes. Thus, the dominant ionization mechanism transfers from tunnelling ionization (TI) to multiphoton ionization (MPI). The calculated J_{in} in Figure 3B indicates reaching its maximum value at z = 193 μm and decaying down to zero at z = 385 μm, while the total net current $J = J_{out} - J_{in}$ in theory (blue dashed line) agrees pretty well with the measured data in the experiment (solid red sphere). Detailed calculation of J_{out} and J_{in} is provided in Appendix A.

Furthermore, the particle-in-cell (PIC) algorithm [41] is employed to simulate the experiment, scanning the laser focal positions −90 μm, 0 μm, 193 μm, 385 μm with respect to the copper wire's surface. The simulation is equipped with parameters at the experimental conditions: laser wavelength of 1030 nm, pulse duration of 400 fs, focal spot size of 10 μm, Rayleigh range of 305 μm, and in a tungsten target, employing a time interval of 10 fs. The panels in the left column of Figure 4 illustrate the distribution of the laser electric field E_y around the wire, showing the beam focus located at various positions (with respect to the surface). Meanwhile, the corresponding photo-electron distributions are

displayed in the right panels. (i) When the focus is at position z = −90 μm, the hot electrons exhibit a homogenous divergence feature in all directions. At this stage, the inward flow current component J_{in} is zero. (ii) As the focus moves to the wire surface (z = 0 μm), the hot electrons distribution keeps homogenous, while the outward current J_{out} reaches the maximum, but J_{in} remains small and negligible. (iii) At focal position 193 μm, the hot electron distribution changes significantly, exhibiting an electron-vacant region near the focus, with a distinct "bifurcation" pattern. This feature is regarded as the secondary ionization process, associated with J_{in} attaining its maximal backward flow to the surface. (iv) When the focus proceeds to position 385 μm, the electron density around the wire surface diminishes considerably down to zero, since both J_{out} and J_{in} decrease as the focus moves away from the surface, reducing the laser beam intensity significantly.

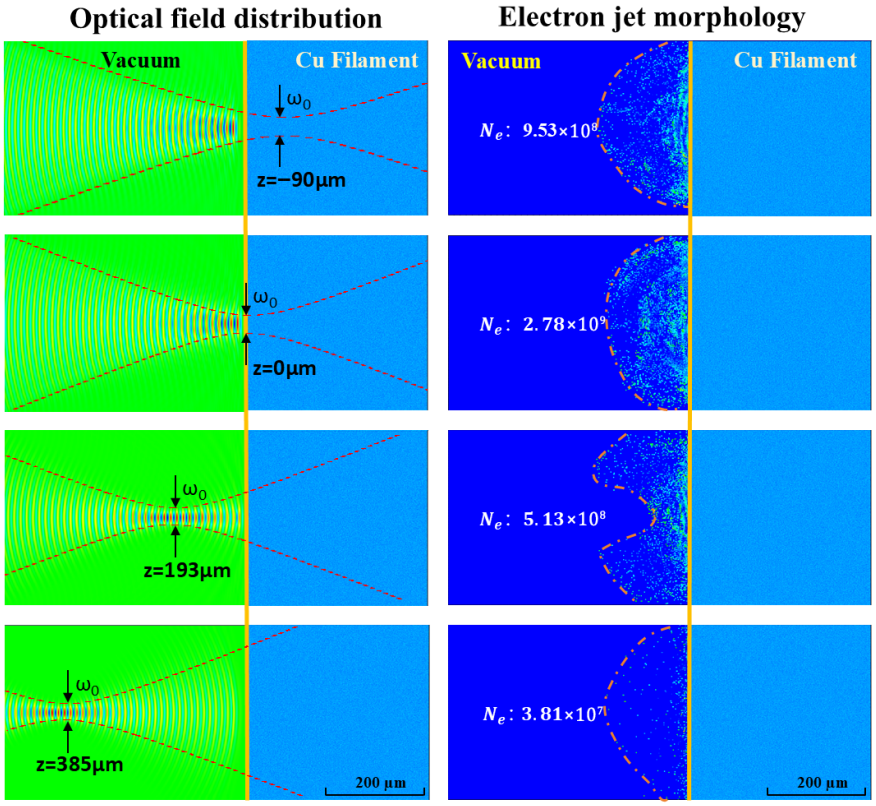

Figure 4. The Monte Carlo collision particle-in-cell (MCC-PIC) model is implemented to simulate the experimental data; both the optical field distribution and the electron jet morphology under various beam intensities are presented by 4 different panels. In the left panels, the beam waist positions with respect to the surface of the copper filament are shown, and the red dashed line represents the laser beam propagation contour. In the right panels, the orange dot-dashed lines represent the contour of the electron jet. More remarkably, when the focus is located exterior to the surface and close enough (in the third row), an electron-vacant region is observed near the beam focus. This reveals a potential mechanism whereby the inward-flowing electron current cancels out the initial outward photoemission. N_e in the plot gives the number of photoelectrons generated by a single laser pulse.

The above electron distribution features (i) to (iv) demonstrate that the PIC simulation is in excellent agreement with the experimental result. Notably, the deformed electron distribution and "bifurcation" pattern at position z = 193 μm is consistent with the schematic illustration depicted in Figure 1B, interpreted by the secondary-ionization and electron inward fluxing scheme. Furthermore, the normal average current from the simulation is approximately 20% higher than the experiment. This discrepancy may be attributed

to the competition among different nonlinear absorption mechanisms, preventing the achievement of the theoretical limit. For the case where the beam focus is located on the target surface, the typical energy range of hot electrons could be derived, exhibiting a broad spectral feature, from several tens to several hundreds of keV, reproducing the experimental findings (inserted curve in Figure 1).

4. Conclusions

In summary, this work reveals, besides the laser beam intensity, how the beam focal position would influence the photo-electron excitation behaviour and dynamics at the metallic filament target. We carried out a systematic experiment to measure the current flow to calibrate the observed phenomena, and in the meantime, established a theoretical model based on secondary excitation and PIC algorithm to simulate the observed feature, aiming to explore the underlying dynamic mechanism, which was not well understood in previous works. Our analysis attributes the asymmetric feature in exterior/interior foci to the secondary-ionization-driven electron backflow, which cancels the outward current and causes polarity reversal. The simulation exhibits excellent agreement with the experimental data. The excitation scheme proposed in this study refines and expands the understanding of electron excitation behaviour in defocused laser–solid interaction systems, elucidating the essential factors which determine the hot electron distribution and plasma jet dynamics in the laser–metal interaction.

Author Contributions: Conceptualization, D.L.; Methodology, D.L.; Software, D.L. and B.L.; Validation, D.L.; Formal analysis, D.L. and B.L.; Investigation, D.L. and B.L.; Resources, B.L.; Data curation, D.L.; Writing—original draft, D.L.; Writing—review & editing, B.L.; Visualization, D.L.; Supervision, B.L.; Project administration, B.L.; Funding acquisition, B.L. All authors have read and agreed to the published version of the manuscript.

Funding: National Natural Science Foundation of China (grant No. 11975299).

Informed Consent Statement: Informed consent was obtained from all subjects involved in the study.

Data Availability Statement: The raw data supporting the conclusions of this article will be made available by the authors on request.

Acknowledgments: The authors thank the technical support from and invaluable discussion with the colleagues in the group of photon diagnostics, Shanghai Advanced Research Institute (SARI), Chinese Academy of Sciences (CAS), and are grateful for the support from Shanghai Soft X-ray Free-Electron Laser Facility (SXFEL), Chinese Academy of Sciences (CAS). The following funding is acknowledged: National Natural Science Foundation of China (grant No. 11975299).

Conflicts of Interest: The authors declare no conflicts of interest.

Appendix A

This appendix provides more details for the theoretical calculation in the main text, including formulas and parameter definitions as follows: the outward excitation efficiency (f_{out}), the excitation current (J_{out}), the ionization rate at the focal point (w_{in}), and the inward flow current (J_{in}).

The outward excitation efficiency f_{out} emerges as the macroscopic outcome of several competitive mechanisms. As the laser intensity varies along the beam propagation direction z, the dominant absorption and ionization mechanisms change accordingly. Within the laser intensity range carried out in the experiment, the primary radiation absorption mechanisms include inverse bremsstrahlung (IB) absorption, resonant absorption (RA), vacuum heating (VH), and Joule heating (JB) [2–7].

The efficiency of IB absorption can be calculated by:

$$f_{ib} = 1 - exp\left(-\frac{32}{15}\frac{V_{e_i}(n_{cr})}{c}L_n\right) \quad \text{(A1)}$$

where $v_{e_i}(n_{Cr}) \approx 3.64 \times 10^{-6}\frac{Zn_{cr}ln\Lambda}{T_e^{2/3}}$ is the electron-ion collision frequency (Coulomb logarithm $\ln\Lambda \approx 10$), Z is the atomic number of the material in the target, T_e is the hot electron temperature, n_{Cr} is the plasma density, which could be calculated by $n_{cr} \approx 1.1 \times 10^{21}/\lambda$ (λ is the laser wavelength in microns), L_n is the plasma scale length.

The efficiency of RA can be calculated by:

$$f_{ra} \approx \frac{\varnothing^2(\tau)}{2} \quad \text{(A2)}$$

where $\tau = \left(\frac{\omega L_n}{c}\right)^{\frac{1}{3}} \cdot sin\vartheta$ is a convenient parameter relating the scale length (ω is the angular frequency of the laser), the function ϕ is given by $\phi(\tau) \approx 2.3\tau exp\left(-\frac{2\tau^3}{3}\right)$, ϑ is the incidence angle of the laser beam to the surface of the material.

The efficiency of VH absorption can be calculated by:

$$f_{vh} = \frac{\eta}{2\pi}\frac{v_{soc}^3}{c^3 cos\vartheta} \quad \text{(A3)}$$

where $v_{osc} = c\sqrt{\frac{I_s\lambda^2}{1.3\times10^{18}}}$ is the plasma oscillation frequency.

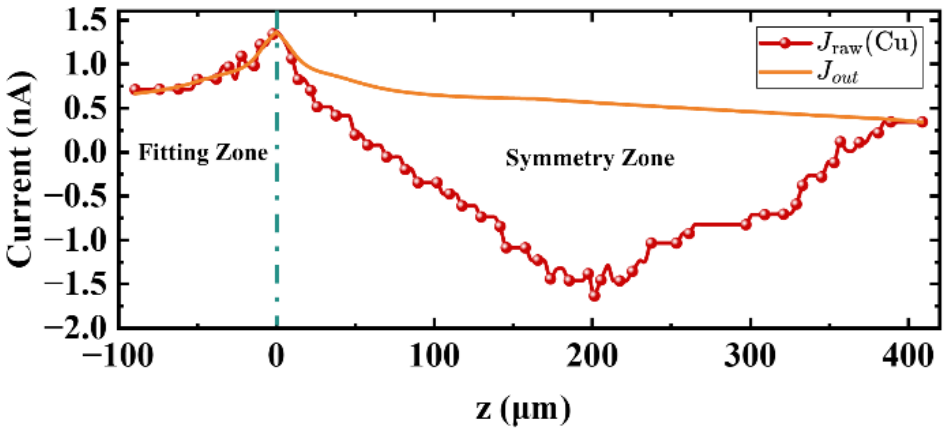

Figure A1. The red dotted line is from the experimental measurement data, and the orange curve represents the fitting curve of J_{out}. The green dashed line indicates the position of the focus on the surface.

The efficiency of J × B absorption can be calculated using the formula:

$$f_{jb} \propto \sqrt{1 + \frac{I_s\lambda^2}{1.37 \times 10^{18}}} - 1 \quad \text{(A4)}$$

As the laser focus is scanned from the interior to the exterior of the material, the surface absorption mechanisms and their respective efficiencies undergo a dynamic evolution. The contributions of the four competing mechanisms are determined by a set of adaptive weighting coefficients k specifically. Eventually, the overall excitation efficiency for the photoemission at the surface can be evaluated by:

$$f_{out} = k_{vh}f_{vh} + k_{ra}f_{ra} + k_{ib}f_{ib} + k_{jb}f_{jb} \quad \text{(A5)}$$

Each weighting coefficient k in Equation (A5) could be determined via fitting the experimental data. During the scanning process, when the focal spot moves from the interior to the surface, i.e., the focal spot is located inside the material, the measured data only involves J_{out} (since $J_{in} = 0$). By implementing various efficiency factors f and fitting parameters k in Equation (A5), then f_{out} would be a fitting parameter in Equation (4) of the main text, a data fitting in this segment (z = 0 to 100 μm), the corresponding fitting curve for J_{out} is obtained.

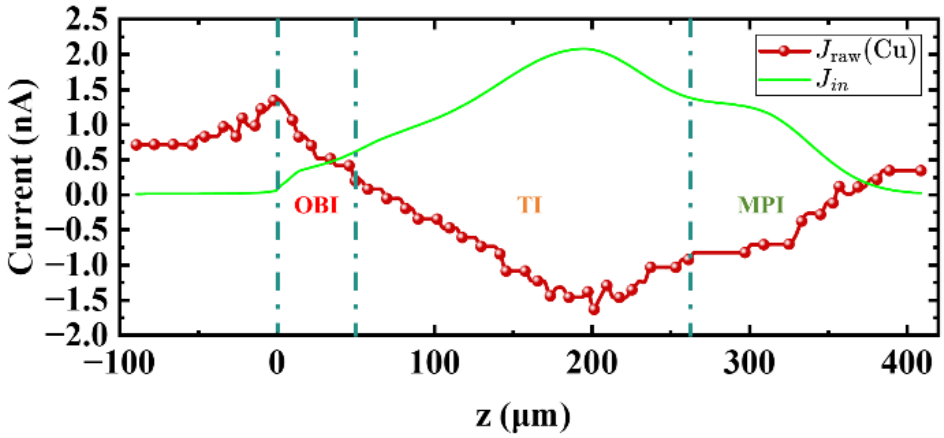

Figure A2. The green curve represents the simulated result of J_{in}, accompanied by the experimental measurements (the red dot-line, same as in Figure A1. The regions labelled OBI, TI, and MPI correspond to the sources of ions, carrying on the secondary ionization to create the back-flowing electrons (current). The green dashed line represents the boundary between different ionization mechanisms.

For the case where the focal spot is located outside the surface, according to the laser beam intensity distribution is symmetric across the surface (indicated by the vertical dot-dash line in Figure A1), J_{out} at various z positions can be derived, that is to say, there is no intrinsic difference compared to J_{out} for interior focus. Consequently, a complete fitted curve of J_{out} spanning the entire experimental range is established.

Moreover, the parameter f_{in} in Equation (5) of the main text could be calculated. w_{in} is defined as the ionization excitation rate at the focal point, f_{in} could also be evaluated at the focal spot (exteriorly), owing to the secondary excitation efficiency associated with the inward-flowing electrons. Since only calculated at the focus, the incident laser beam intensity remains constant during the interaction, while J × B absorption would be the dominant mechanism (f_{jb}).

$$f_{in} \approx f_{jb} \propto \sqrt{1 + \frac{I_p \lambda^2}{1.37 \times 10^{18}}} - 1 \tag{A6}$$

However, scanning the coordinate z would change the beam intensity at the surface, then the ionization rates are modified, generating a different number of ions at the beam focus. This, in turn, would determine the number of back-flowing electrons and influence the dynamics, which could be comprehensively encapsulated within the parameter w_{in}.

More specifically, w_{in} is calculated in a manner analogous to w_{out}, with the only difference lying in the parameter γ. By substituting z = 0 into Equation (3) in the main text, the ionization rate for the second excitation at the focal point can be obtained:

$$w_{in} = \sqrt{\frac{2\pi z}{3 + 3z}} \times \left(\frac{E_0 I_s}{c\epsilon_0}\right)^{\frac{1}{4}} exp\left(-\frac{4}{3}\frac{E_0^2 c\epsilon_0}{\omega I_s}\left[1 - \frac{1}{10}\frac{E_0 c\epsilon_0}{I_s}^2\right]\right) \tag{A7}$$

The theoretical curve for J_{in} is obtained by plugging Equations (A7) and (1) into Equation (5) of the main text. For $z < 0$, J_{in} has no physical significance and is accordingly set to zero, as shown in Figure A2.

References

1. Strickland, D.; Mourou, G. Compression of amplified chirped optical pulses. *Opt. Commun.* **1985**, *55*, 447–449. [CrossRef]
2. Kostyukov, I.Y.; Nerush, E.N. Production and dynamics of positrons in ultrahigh intensity laser-foil interactions. *Phys. Plasmas* **2026**, *23*, 093119. [CrossRef]
3. Vshivkov, V.A.; Naumova, N.M.; Pegoraro, F.; Bulanov, S.V. Nonlinear electrodynamics of the interaction of ultra-intense laser pulses with a thin foil. *Phys. Plasmas* **1998**, *5*, 2727–2741. [CrossRef]
4. Nerush, E.N.; Kostyukov, I.Y.; Ji, L.; Pukhov, A. Gamma-ray generation in ultrahigh-intensity laser-foil interactions. *Phys. Plasmas* **2014**, *21*, 013109. [CrossRef]
5. Kar, S.; Borghesi, M.; Bulanov, S.V.; Key, M.H.; Liseykina, T.V.; Macchi, A.; Mackinnon, A.J.; Patel, P.K.; Romagnani, L.; Schiavi, A.; et al. Plasma jets driven by ultraintense-laser interaction with thin foils. *Phys. Rev. Lett.* **2008**, *100*, 225004. [CrossRef]
6. Mandal, T.; Arora, V.; Moorti, A.; Uphadhyay, A.; Chakera, J.A. Addressing key aspects of J × B driven MeV fast electron generation in ultra-short ultra-intense laser foil interaction. *Phys. Plasmas* **2023**, *30*, 023106. [CrossRef]
7. Vyskočil, J.; Klimo, O.; Weber, S. Simulations of bremsstrahlung emission in ultra-intense laser interactions with foil targets. *Plasma Phys. Control. Fusion* **2018**, *60*, 054013. [CrossRef]
8. Borghesi, M.; MacKinnon, A.J.; Bell, A.R.; Gaillard, R.; Willi, O. Megagauss magnetic field generation and plasma jet formation on solid targets irradiated by an ultraintense picosecond laser pulse. *Phys. Rev. Lett.* **1998**, *81*, 112. [CrossRef]
9. Sentoku, Y.; Ruhl, H.; Mima, K.; Kodama, R.; Tanaka, K.A.; Kishimoto, Y. Plasma jet formation and magnetic-field generation in the intense laser plasma under oblique incidence. *Phys. Plasmas* **1999**, *6*, 2855–2861. [CrossRef]
10. Shoucri, M.; Lavocat-Dubuis, X.; Matte, J.P.; Vidal, F. Numerical study of ion acceleration and plasma jet formation in the interaction of an intense laser beam normally incident on an overdense plasma. *Laser Part. Beams* **2011**, *29*, 315–332. [CrossRef]
11. Nakajima, H.; Tokita, S.; Inoue, S.; Hashida, M.; Sakabe, S. Divergence-free transport of laser-produced fast electrons along a meter-long wire target. *Phys. Rev. Lett.* **2013**, *110*, 155001. [CrossRef]
12. Tokita, S.; Otani, K.; Nishoji, T.; Inoue, S.; Hashida, M.; Sakabe, S. Collimated Fast Electron Emission from Long Wires Irradiated by Intense Femtosecond Laser Pulses. *Phys. Rev. Lett.* **2011**, *106*, 255001. [CrossRef]
13. Davies, J.R.; Bell, A.R.; Tatarakis, M. Magnetic focusing and trapping of high-intensity laser-generated fast electrons at the rear of solid targets. *Phys. Rev. E* **1999**, *59*, 6032–6036. [CrossRef]
14. Mao, J.Y.; Chen, L.M.; Ge, X.L.; Zhang, L.; Yan, W.C.; Li, D.Z.; Liao, G.Q.; Ma, J.L.; Huang, K.; Li, Y.T.; et al. Spectrally peaked electron beams produced via surface guiding and acceleration in femtosecond laser-solid interactions. *Phys. Rev. E—Stat. Nonlinear Soft Matter Phys.* **2012**, *85*, 025401. [CrossRef]
15. Norreys, P.; Batani, D.; Baton, S.; Beg, F.N.; Kodama, R.; Nilson, P.M.; Patel, P.; Pérez, F.; Santos, J.; Scott, R.; et al. Fast electron energy transport in solid density and compressed plasma. *Nucl. Fusion* **2014**, *54*, 054004. [CrossRef]
16. Bell, A.R.; Davies, J.R.; Guerin, S.; Ruhl, H. Fast-electron transport in high-intensity short-pulse laser-solid experiments. *Plasma Phys. Control. Fusion* **1997**, *39*, 653–659. [CrossRef]
17. Freeman, R.R.; Batani, D.; Baton, S.; Key, M.; Stephens, R. The generation and transport of large currents in dense materials: The physics of electron transport relative to fast ignition. *Fusion Sci. Technol.* **2006**, *49*, 297–315. [CrossRef]
18. Yin, J.; Yuan, X.; Zhou, Z.; Pei, G.; Liu, S. Novel electron source based on interaction between high power laser and metal wire. *High Power Laser Part. Beams* **2021**, *33*, 094003.
19. Kuratov, A.S.; Brantov, A.V.; Bychenkov, V.Y. Modeling of laser generation and propagation of electron bunch along thin irradiated wire. *Bull. Lebedev Phys. Inst.* **2018**, *45*, 346–349. [CrossRef]
20. Li, Y.T.; Yuan, X.H.; Xu, M.H.; Zheng, Z.Y.; Sheng, Z.M.; Chen, M.; Ma, Y.Y.; Liang, W.X.; Yu, Q.Z.; Zhang, Y.; et al. Observation of a Fast Electron Beam Emitted along the Surface of a Target Irradiated by Intense Femtosecond Laser Pulses. *Phys. Rev. Lett.* **2006**, *96*, 165003. [CrossRef] [PubMed]
21. Tokita, S.; Sakabe, S.; Nagashima, T.; Hashida, M.; Inoue, S. Strong sub-terahertz surface waves generated on a metal wire by high-intensity laser pulses. *Sci. Rep.* **2015**, *5*, 8268. [CrossRef]
22. Zhuo, H.B.; Zhang, S.J.; Li, X.H.; Zhou, H.Y.; Li, X.Z.; Zou, D.B.; Yu, M.Y.; Wu, H.C.; Sheng, Z.M.; Zhou, C.T. Terahertz generation from laser-driven ultrafast current propagation along a wire target. *Phys. Rev. E* **2017**, *95*, 013201. [CrossRef]
23. Wang, K.; Mittleman, D.M. Guided propagation of terahertz pulses on metal wires. *J. Opt. Soc. Am. B* **2005**, *22*, 2001–2008. [CrossRef]
24. Zeng, Y.; Zhou, C.; Song, L.; Lu, X.; Li, Z.; Ding, Y.; Bai, Y.; Xu, Y.; Leng, Y.; Tian, Y.; et al. Guiding and emission of milijoule single-cycle THz pulse from laser-driven wire-like targets. *Opt. Express* **2020**, *28*, 15258–15267. [CrossRef] [PubMed]

25. Tian, Y.; Liu, J.; Bai, Y.; Zhou, S.; Sun, H.; Liu, W.; Zhao, J.; Li, R.; Xu, Z. Femtosecond-laser-driven wire-guided helical undulator for intense terahertz radiation. *Nat. Photonics* **2017**, *11*, 242–246. [CrossRef]
26. Wilks, S.C.; Kruer, W.L. Absorption of ultrashort, ultra-intense laser light by solids and overdense plasmas. *IEEE J. Quantum Electron.* **1997**, *33*, 1954–1968. [CrossRef]
27. Keldysh, L.V. Ionization in the field of a strong electromagnetic wave. *J. Exp. Theor. Phys.* **1964**, *47*, 1945.
28. Kasperczuk, A.; Pisarczyk, T.; Badziak, J.; Miklaszewski, R.; Parys, P.; Rosinski, M.; Wolowski, J.; Stenz, C.; Ullschmied, J.; Krousky, E.; et al. Influence of the focal point position on the properties of a laser-produced plasma. *Phys. Plasmas* **2007**, *14*, 102706. [CrossRef]
29. Zhang, P.; Ji, Y.J.; Lai, X.M.; Bian, B.M.; Li, Z.H. Peak polarity overturn for charged particles in laser ablation process. *J. Appl. Phys.* **2006**, *100*, 013303. [CrossRef]
30. Boroumand, N.; Thorpe, A.; Parks, A.M.; Brabec, T. Keldysh ionization theory of atoms: Mathematical details. *J. Phys. B At. Mol. Opt. Phys.* **2022**, *55*, 213001. [CrossRef]
31. Karnakov, B.M.; Mur, V.D.; Popruzhenko, S.V.E.; Popov, V.S. Current progress in developing the nonlinear ionization theory of atoms and ions. *Physics-Uspekhi* **2015**, *58*, 3–32. [CrossRef]
32. Mishima, K.; Nagaya, K.; Hayashi, M.; Lin, S.H. Theoretical studies of high-power laser ionization of molecules in the tunneling region. *Phys. Rev. A—At. Mol. Opt. Phys.* **2004**, *70*, 063414. [CrossRef]
33. Bauer, J.H. Keldysh theory re-examined. *J. Phys. B At. Mol. Opt. Phys.* **2016**, *49*, 145601. [CrossRef]
34. Zhao, S.F.; Liu, L.; Zhou, X.X. Multiphoton and tunneling ionization probability of atoms and molecules in an intense laser field. *Opt. Commun.* **2014**, *313*, 74–79. [CrossRef]
35. Sheng, Z.M.; Weng, S.M.; Yu, L.L.; Wang, W.M.; Cui, Y.Q.; Chen, M.; Zhang, J. Absorption of ultrashort intense lasers in laser–solid interactions. *Chin. Phys. B* **2015**, *24*, 015201. [CrossRef]
36. Bloembergen, N. Fundamentals of laser-solid interactions. In *AIP Conference Proceedings*; American Institute of Physics: College Park, MD, USA, 1979; Volume 50, pp. 1–9.
37. Chen, L.M.; Zhang, J.; Dong, Q.L.; Teng, H.; Liang, T.J.; Zhao, L.Z.; Wei, Z.Y. Hot electron generation via vacuum heating process in femtosecond laser–solid interactions. *Phys. Plasmas* **2001**, *8*, 2925–2929. [CrossRef]
38. Santala, M.I.K.; Zepf, M.; Watts, I.; Beg, F.N.; Clark, E.; Tatarakis, M.; Krushelnick, K.; Dangor, A.E.; McCanny, T.; Spencer, I.; et al. Effect of the plasma density scale length on the direction of fast electrons in relativistic laser-solid interactions. *Phys. Rev. Lett.* **2000**, *84*, 1459–1462. [CrossRef]
39. Davies, J.R. Laser absorption by overdense plasmas in the relativistic regime. *Plasma Phys. Control. Fusion* **2008**, *51*, 014006. [CrossRef]
40. Von der Linde, D.; Sokolowski-Tinten, K.; Bialkowski, J. Laser–solid interaction in the femtosecond time regime. *Appl. Surf. Sci.* **1997**, *109–110*, 1–10. [CrossRef]
41. Arber, T.D.; Bennett, K.; Brady, C.S.; Lawrence-Douglas, A.; Ramsay, M.G.; Sircombe, N.J.; Gillies, P.; Evans, R.G.; Schmitz, H.; Bell, A.R.; et al. Contemporary particle-in-cell approach to laser-plasma modelling. *Plasma Phys. Control. Fusion* **2015**, *57*, 113001. [CrossRef]

Disclaimer/Publisher's Note: The statements, opinions and data contained in all publications are solely those of the individual author(s) and contributor(s) and not of MDPI and/or the editor(s). MDPI and/or the editor(s) disclaim responsibility for any injury to people or property resulting from any ideas, methods, instructions or products referred to in the content.